

Unconventional stabilization mechanisms and emergent superconductivity in scandium polychlorides under extreme conditions

Ziji Shao(邵子霁), Maosheng Miao(苗茂生), Wendi Zhao(赵文迪), Mengxi Wang(王梦溪), Yingmei Zhu(朱英梅), Changqiu Yu(于长秋), Defang Duan(段德芳), and Tiejun Zhou(周铁军)

Citation: Chin. Phys. B, 2025, 34 (**11**): 116201. DOI: 10.1088/1674-1056/ae0431
http://cpb.iphy.ac.cn; http://iopscience.iop.org/cpb

What follows is a list of articles you may be interested in

Theoretical investigation on the H sublattice in CaH_6 and energetic performance

Zhihong Huang(黄植泓), Nan Li(李楠), Jun Zhang(张俊), Xiuyuan Li(李修远), Zihuan Peng(彭梓桓), Chongwen Jiang(江崇文), and Changqing Jin(靳常青)

Chin. Phys. B, 2025, 34 (**8**): 086202. DOI: 10.1088/1674-1056/ade1c3

A novel metastable structure and superconductivity of hydrogen-rich compound CdH_6 under pressure

Yan Yan(闫岩), Chengao Jiang(蒋成澳), Wen Gao(高稳), Rui Chen(陈蕊), Xiaodong Yang(杨晓东), Runru Liu(刘润茹), Lihua Yang(杨丽华), and Lili Wang(王丽丽)

Chin. Phys. B, 2025, 34 (**8**): 086201. DOI: 10.1088/1674-1056/add902

Band gap engineering and vibrational properties of van der Waals semiconductor $ZnPSe_3$ under compression

Rouqiong Su(苏柔琼), Yuying Li(李玉莹), Chunhua Chen(陈春华), Yifang Yuan(袁亦方), and Haizhong Guo(郭海中)

Chin. Phys. B, 2025, 34 (**6**): 066205. DOI: 10.1088/1674-1056/adcaa2

Structural regulation and optical behavior of zero-dimensional Cu(I)-based organometallic halides under pressure

Runnan Ye(叶润楠), Jingtian Wang(王敬天), Jiayi Yang(杨佳毅), Xuchen Wang(王旭晨), Junce Lei(雷钧策), Wenya Zhao(赵文雅), Yufan Meng(孟雨凡), Guanjun Xiao(肖冠军), and Bo Zou(邹勃)

Chin. Phys. B, 2025, 34 (**6**): 066204. DOI: 10.1088/1674-1056/adc193

Stoichiometric change and solid decomposition in Ca-S compounds under high pressure

Yang Lv(吕阳), Jian-Fu Li(李建福), Zhao-Bin Zhang(张钊彬), Yong Liu(刘勇), Jia-Nan Yuan(袁嘉男), Jia-Ni Lin(林佳妮), and Xiao-Li Wang(王晓丽)

Chin. Phys. B, 2025, 34 (**4**): 046202. DOI: 10.1088/1674-1056/adb38e

---

SPECIAL TOPIC — Structures and properties of materials under high pressure

Unconventional stabilization mechanisms and emergent superconductivity in scandium polychlorides under extreme conditions

Ziji Shao(邵子雾)[1], Maosheng Miao(苗茂生)[2], Wendi Zhao(赵文迪)[3], Mengxi Wang(王梦溪)[4], Yingmei Zhu(朱英梅)[4], Changqiu Yu(于长秋)[1], Defang Duan(段德芳)[3,†], and Tiejun Zhou(周铁军)[1,‡]

[1] *College of Electronics And Information, Hangzhou Dianzi University, Hangzhou* 310018, *China*

[2] *Department of Chemistry and Biochemistry, California State University Northridge, Los Angeles, California* 91330, *United States*

[3] *International Center for Computational Method and Software and State Key Laboratory of Superhard Materials, College of Physics, Jilin University, Changchun* 130012, *China*

[4] *State Key Laboratory for Spintronics Devices and Technologies, Hangzhou* 311300, *China*

(Received 25 June 2025; revised manuscript received 15 August 2025; accepted manuscript online 8 September 2025)

Using first-principles evolutionary crystal structure prediction, we systematically investigate scandium polychlorides across 50–300 GPa, predicting multiple thermodynamically stable phases ScCl, $ScCl_2$, $ScCl_3$, $ScCl_5$, and $ScCl_7$ with unconventional stoichiometries. The exceptional stability of these compounds stems from the mutually compatible crystal orbitals of the Sc and Cl sublattices, strong ionic interactions, and the formation of Cl–Cl homobonds. These factors play critical roles in stabilizing scandium chloride compounds with various unconventional stoichiometries. Notably high-pressure novel ScCl phases with $P6_3/mmc$ and Pm-3m symmetries can be metastable at ambient pressure upon decompression and convert into superconductive electrides. Pm-3-$ScCl_7$ exhibits significant pressure-modulated superconductivity, featuring an enhancement of T_c to 10.91 K at a low pressure of 75 GPa. In addition, the universal superconductivity found in the Pm-3 structured chlorides suggests a promising structural prototype for pressure-tunable superconductors.

Keywords: high pressure, first-principles calculation, crystal structure prediction

PACS: 62.50.–p, 74.62.Fj, 81.40.Vw, 91.60.Gf

DOI: 10.1088/1674-1056/ae0431 **CSTR:** 32038.14.CPB.ae0431

1. Introduction

The stability and structure of metal–nonmetal systems with significantly different electronegativities are fundamentally determined by valence electron configurations at ambient pressure. Within the conventional ionic bonding model, complete electron transfers from electropositive metallic atoms to electronegative nonmetallic atoms facilitate ionic interactions. However, pressure can effectively alter the chemical characteristics of elements and their interactions, leading to the emergence of novel phases and unconventional stoichiometric compounds with unexpected physical properties.[1]

As a group VIIA element with high electronegativity, chlorine typically adopts a -1 oxidation state by acquiring one electron when forming compounds with metals at atmospheric pressure. In these conventional ionic compounds, chlorine atoms adopt closed-shell electronic configurations (Cl^-) stabilized as atomic anions, as exemplified by alkali metal chlorides (NaCl and KCl),[2,3] alkali earth metal chlorides ($CaCl_2$ and $BaCl_2$),[4,5] transition metal chlorides ($ScCl_3$, YCl_3, $RuCl_3$, and $FeCl_3$),[6–8] rare earth metal chlorides ($LaCl_3$),[9] and so on. Even in unconventional stoichiometric layered metal chlorides such as ScCl, YCl, and $CrCl_2$, the chlorine persists in atomic anionic states under ambient conditions.[6,10] Remarkably, high-pressure theoretical and experimental investigations[11,12] have revealed several unconventional stoichiometric compounds and even multiple structure evolution behaviors like metallic carbides Na–C system, where carbons experience a transition of isolated anions → tetramers → extended chains → pentagonal and hexagonal rings under pressure.[13] For chlorine-rich compounds, chlorine atoms deviate from conventional anionic states to form diverse chlorine structural motifs such as linear Cl_3^- units, monatomic chlorine chains, and layered configurations.

It is reported that unconventional stoichiometric compounds, $NaCl_3$ and KCl_3, are stable in the $Pnma$ structure above 20 GPa and 1.3 GPa, respectively, containing almost linear asymmetric Cl_3^- units, in which the central Cl atom is nearly neutral in charge and terminal atoms are negative. Upon compression, $NaCl_3$ and KCl_3 convert to A15 structure with Pm-3n symmetry above 50 GPa, and novel chlorine-rich $NaCl_7$ and KCl_7 with Pm-3 space group, derivative structure of the A15, become thermodynamically stable above 143 GPa

†Corresponding author. E-mail: duandf@jlu.edu.cn

‡Corresponding author. E-mail: tjzhou@hdu.edu.cn

© 2025 Chinese Physical Society and IOP Publishing Ltd. All rights, including for text and data mining, AI training, and similar technologies, are reserved.

and 225 GPa, respectively. These high-symmetry cubic phases feature extended chains covalently connected along three perpendicular axes with interatomic distances (e.g., 2.06 Å in *Pm*-3*n*-$NaCl_3$ at 200 GPa) comparable to 1.99 Å in Cl_2 molecular units.[11,12] $CaCl_2$ experiences a *Pnma*→*P*-62*m* →*Pnma* phase transition. In addition, unstoichiometric CaCl, Ca_5Cl_6, Ca_3Cl_4, and $CaCl_3$ are also discovered.[14,15] Long sought monovalent calcium compound CaCl can be stabilized above 18 GPa with fcc structure and convert to ferromagnetic bcc CaCl above 40 GPa.[14] Cubic $CaCl_3$ with A15 structure stable at 33.5 GPa is found to possess Rubik's cubic Fermi surface.[15] Parallel investigations on the Y–Cl system up to 60 GPa uncovered the Y_2Cl_3 electride above 10 GPa, where Cl atoms form atomic planes between Y layers along the (001) lattice plane. The interstitial electrons are located between Y–Cl layers and connect with Cl atoms along the [001] direction.[16]

These pressure-induced unconventional stoichiometries and various Cl motifs challenge classical valence-based stability concepts, necessitating a comprehensive investigation of their formation mechanisms. The sublattice interaction theory promoted recently provides critical insights into crystal architecture under high pressure, particularly for polyhydrides.[17,18] In such a typical metal–nonmetal system, interstitial electrons from metal sublattices occupy quasi-atomic orbitals that template hydrogen sublattice configurations, exemplified by the early transition metal polyhydrides ScH_n ($n = 6$, 9, and 10), where interstitial electrons from Sc sublattices stabilize high-symmetry H cages.[19–21]

Under ambient pressure, stoichiometric scandium chloride $ScCl_3$, stabilized in the *R*-3 space group, features three stacking $ScCl_3$ layers consisting of Sc^{3+} cations and Cl^- anions.[6] A recent theoretical investigation identified *R*-3*m*-ScCl as a novel magnetic electride, with stacked folded Sc–Cl monolayers and interlayer-localized interstitial electrons.[6] Until now, the high-pressure phase diagram of the Sc–Cl system has rarely been investigated. Given chlorine's comparable electronegativity to hydrogen under pressure (9.1 for Cl and 6.1 for H at 300 GPa[22]), multiple Cl configurations beyond ionic bonding constraints are expected in the high-pressure Sc–Cl system with exotic properties.

Herein, we present a systematic investigation of scandium polychlorides $ScCl_n$ ($n = 1$–10) from 50 GPa to 300 GPa and reveal multiple stable stoichiometries (ScCl, $ScCl_2$, $ScCl_3$, $ScCl_5$, and $ScCl_7$) with distinct stabilization mechanisms. Increasing Cl content drives sequential evolution from atomic anions (ScCl, $ScCl_2$) through Cl_2 dimers ($ScCl_3$) to extended Cl covalent chains ($ScCl_5$, $ScCl_7$), accompanied by complex stabilization mechanisms: sublattice orbital interactions, conventional ionic bonding, and pressure-enhanced Cl–Cl homobonding. Notably, the high-pressure phases $P6_3/mmc$-ScCl and *Pm*-3*m*-ScCl, thermodynamically stable in the pressure range of 50–100 GPa and 100–300 GPa, can be decompressed to ambient pressure and become superconductive electrides. High-pressure phase *Pm*-3-$ScCl_7$ exhibits an enhanced T_c of 10.91 K at 75 GPa, comparable to the T_c of 13.03 K of Cl_2 solid at 380 GPa.[23]

2. Calculation methods

Variable composition searches of the Sc–Cl stable stoichiometries at 50 GPa, 100 GPa, 200 GPa, and 300 GPa were conducted through the evolutionary algorithm USPEX[24,25] code with respect to Sc and Cl elements (Fig. S1). Then, we performed the fixed composition searches on the $ScCl_n$ ($n = 1$–10) stable crystal structures from 50 GPa to 300 GPa within 2–4 formula units to further confirm the results of the variable composition searches. The first generation of 60 structures was produced randomly, and the subsequent generations of 30 structures were obtained by applying heredity, transmutation, softmutation, and lattice mutation operations, with probabilities of 60%, 10%, 20% and 10%, respectively. The predictions stopped if the best structure did not change for 20 generations. Structural relaxations, electronic properties, and total energies were calculated in the framework of density functional theory (DFT) with Perdew–Burke–Ernzerhof parameterization (PBE) of the generalized gradient approximation (GGA)[26] as implemented in the Vienna *ab initio* simulation package (VASP).[27] The all-electron projector augmented wave (PAW)[28] method was used to describe the ion–electron interactions with $3s^23p^5$ and $3s^23p^63d^14s^2$ as valence for Cl and Sc, respectively. We employed an 800 eV plane-wave energy cutoff. Monkhorst–Pack meshes for Brillion zone sampling with resolutions of $2\pi \times 0.03$ Å^{-1} and $2\pi \times 0.025$ Å^{-1} were used for structure optimization and electronic property calculations, respectively. Lattice dynamics and electron–phonon coupling (EPC) were characterized by density functional perturbation theory (DFPT) as implemented in the Quantum-ESPRESSO package.[29] A kinetic energy cutoff of 80 Ry was adopted with ultrasoft pseudopotentials for Cl and Sc. Methfessel–Paxton smearing method[30] with the smearing of 0.03 is chosen after convergence tests (Fig. S18). The numbers of *k*-points and *q*-points were $24 \times 24 \times 24$ and $6 \times 6 \times 6$ for $P6_3/mmc$-ScCl, *Pm*-3*m*-ScCl, $I4/mmm$-$ScCl_2$ and *Pm*-3-$ScCl_7$, $20 \times 20 \times 8$ and $5 \times 5 \times 2$ for *Cmcm*-$ScCl_3$, $8 \times 20 \times 20$ and $2 \times 5 \times 5$ for *Amm*2-$ScCl_3$, and $12 \times 12 \times 8$ and $3 \times 3 \times 2$ for *P*-3-$ScCl_5$. The critical temperature T_c was estimated through the Allen−Dynes–modified McMillan formula as follows:[31]

$$T_c = \frac{\omega_{\log}}{1.2} \exp\left[-\frac{1.04(1+\lambda)}{\lambda - \mu^*(1+0.62\lambda)}\right], \tag{1}$$

where μ^* is the effective Coulomb repulsion, which is usually taken as 0.1–0.13, the EPC parameter λ and the logarithmic

average frequency $\omega_{\log}$ are respectively calculated as follows:

$$\lambda = 2\int_0^{\infty} \frac{\alpha^2 F(\omega)}{\omega} \mathrm{d}\omega, \tag{2}$$

$$\omega_{\log} = \frac{2}{\lambda}\int_0^{\infty} \frac{\alpha^2 F(\omega)\ln(\omega)}{\omega} \mathrm{d}\omega. \tag{3}$$

3. Results and discussion

3.1. Stabilities and structures

To investigate the thermodynamic stability of Sc–Cl systems, the formation enthalpies (ΔH_{f}) of all the predicted polychlorides $ScCl_n$ ($n = 1$–10) are calculated in a pressure range of 50–300 GPa. The known structures $P6_3/mmc$-Sc, $P6_522$-Sc, *Cmca*-Cl, and *Immm*-Cl are used as references.[32,33] The convex hull built by ΔH_{f} [Figs. 1(a)–1(f)] reveals stable pressure regions for multiple stoichiometries. From 50 GPa to 100 GPa, ScCl, $ScCl_2$, and $ScCl_3$ lie on the convex hull. Compounds ScCl and $ScCl_2$ remain thermodynamically stable until 300 GPa, while $ScCl_3$ decomposes above 250 GPa. Notably, polychlorides $ScCl_7$ and $ScCl_5$ start to locate on the convex hull at 150 GPa and 200 GPa, respectively, and remain stable until 300 GPa. The pressure-dependent phase transitions and crystal structures for each stable $ScCl_n$ ($n = 1$, 2, 3, 5, and 7) are shown in Figs. 1(g) and 2, respectively. The structure parameters can be found in Table S1 of the supporting information. Despite the pronounced electronegativity difference between Sc (+3) and Cl (−1), the stability of scandium chlorides under pressure transcends conventional valence considerations.

For the case of monochloride ScCl, a hexagonal $P6_3/mmc$ phase is stable from 50 GPa to 100 GPa, succeeded by a CsCl-type $Pm\text{-}3m$ structure above 100 GPa, which is iso-structural with high-pressure calcium chloride CaCl.[14] The dichloride $ScCl_2$ maintains its $I4/mmm$ structure throughout the investigated pressure range, featuring characteristic tetragonal $ScCl_8$ units arranged in stacked layers along the *c*-axis. Within this structure, Sc atoms exhibit four-fold chlorine coordination. The electronic localization function (ELF) shows no electron accumulation between Cl–Cl and Cl–Sc in ScCl and $ScCl_2$ [Figs. S2(a)–S2(c)], indicating the ionic interactions. However, as typical metal–nonmetal systems, the numbers of nonmetal Cl atoms in ScCl and $ScCl_2$ with Sc:Cl ratios of 1:1 and 1:2 are insufficient to satisfy the closed-shell stable structure of metal Sc atoms. Therefore, the orbital interactions between metal and nonmetal sublattices are also considered, in which the electrons migrate from quasi-atomic orbitals in metal sublattices to empty states of non-metal atoms located at the interstitial sites.

The 3D ELF of the Sc sublattices of $P6_3/mmc$-ScCl, $Pm\text{-}3m$ ScCl, and $I4/mmm$-$ScCl_2$, with the addition of Cl atoms under pressures, are displayed in Figs. S3 and S4. The interstitial electrons are found in the Sc sublattices and occupy the crystal orbitals, well matching the positions of the Cl atoms in the original structure, implying that these extra electrons will naturally dope the unoccupied crystal orbitals of the Cl atoms and enhance the structural stability.[17] Furthermore, the underlying mechanism through which inter-sublattice ionic interactions enhance structural stability can be elucidated by systematically examining the electronic band structure evolution in the vicinity of the Fermi level.[17,18] Band structures and elemental projected electronic density of states (PDOS) for isolated element sublattices and binary compounds in $P6_3/mmc$-ScCl, $Pm\text{-}3m$-ScCl, and $I4/mmm$-$ScCl_2$ phases at different pressures are calculated (Figs. S5 and S6). The electron bands of Sc and Cl sublattices exhibit significant overlap near the Fermi level, where electrons originating from the Sc sublattice naturally dope into the unoccupied orbitals of the Cl sublattice, thereby lowering the energy of these orbitals relative to the Fermi level and consequently enhancing the structural stability. The PDOS near the Fermi level shows similar trends, and the large overlap between Sc and Cl states before and after the sublattice combination indicates the position coincidence of interstitial electron and non-metal sites.

At the same time, the stability evolution under pressure is also investigated. The pressure-induced phase transition manifests distinct coordination environments for interstitial electrons in ScCl. For hexagonal ScCl, electrons localize at Sc triangular pyramid centers with six-fold Sc coordination. The high-pressure cubic phase exhibits electronic localization with eight-fold Sc coordination mainly at the center of the simple cubic Sc sublattice. Generally, the increase in pressure will increase the coordination number of interstitial local electrons, which explains why ScCl tends to crystallize in the cubic phase at higher pressure. Furthermore, for $P6_3/mmc$-ScCl, pressure induces a dimension reduction of interstitial electron shape from 3D framework to 2D layers with c/a ratio expansion from 2.33 to 2.45 from 50 GPa to 200 GPa, signifying weakened interlayer interactions and the pressure-induced phase instability. $I4/mmm$-$ScCl_2$ exhibits a body center Sc framework, with interstitial electrons mainly occupying octahedral sites at 50 GPa in a pattern matching Cl positions. Progressive compression transforms these isolated electron regions into an interconnected network, with additional localization at tetrahedral sites within the Sc lattice, functionally similar to Cl anions, and strengthens the stability of the high-pressure $ScCl_2$ phase as pressure increases. The PDOSs show that the energetic reduction near the Fermi level after the sublattice combination gradually increases as the pressure is increased from 50 GPa to 300 GPa, indicating the pressure-strengthened stability of $ScCl_2$.

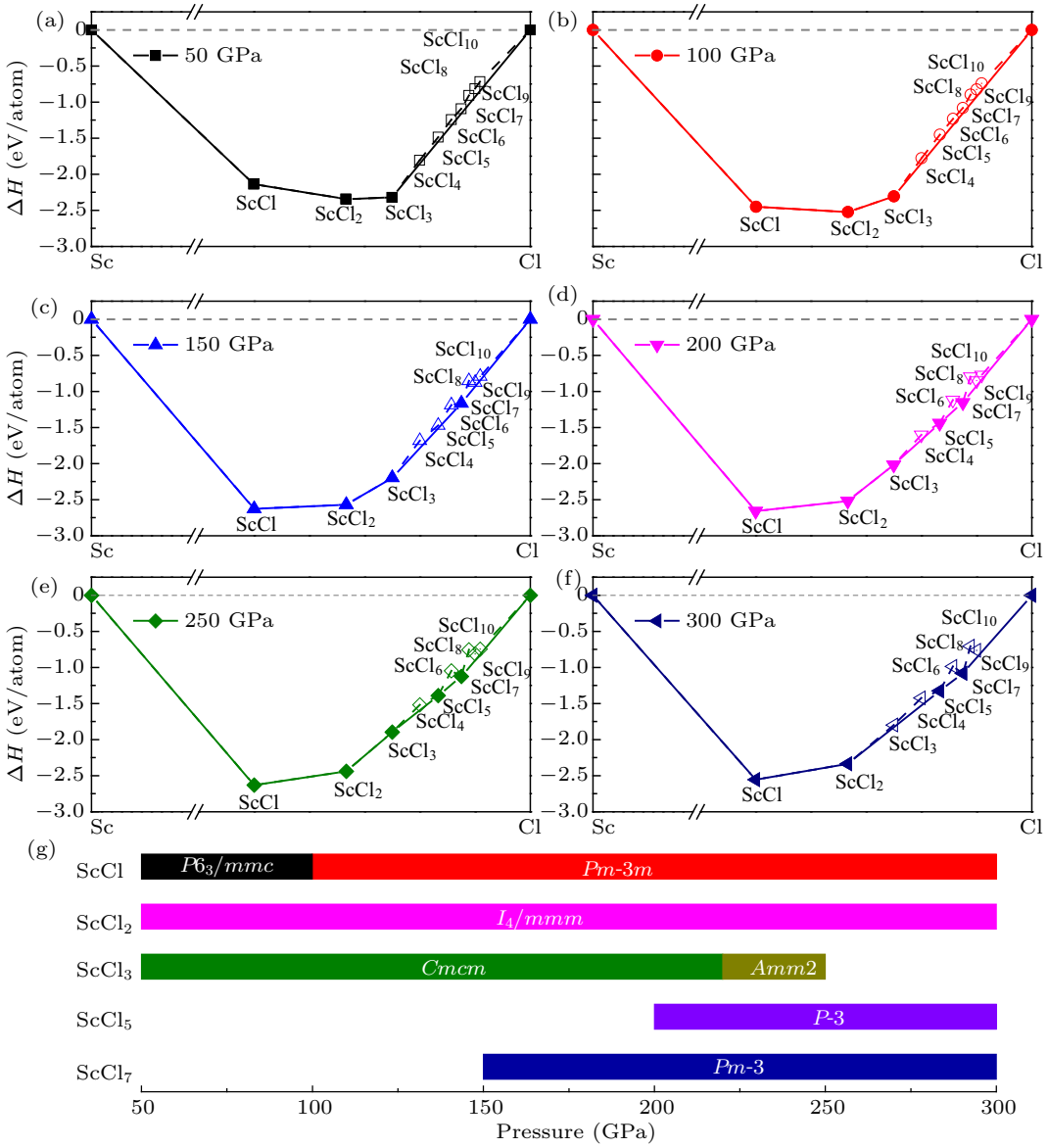


Fig. 1. (a)–(f) The enthalpies of formation of $ScCl_n$ (n = 1–10) with respect to Sc and Cl_2 at 50–300 GPa. (g) The phase transition series of stable compounds ScCl, $ScCl_2$, $ScCl_3$, $ScCl_5$, and $ScCl_7$.

$ScCl_3$ is first stable as a *Cmcm* structure from 50 GPa to 220 GPa and followed by the *Amm*2 structure. The *Cmcm* phase features base-shared triangular prism chains along the *b*-axis composed of $ScCl_6$ units. Upon pressure-induced transformation, the *Amm*2 phase develops a complex architecture where two distorted $ScCl_8$ units form spatial translation units through face-sharing, organizing into layers A and B, shown in Fig. 2(e), alternately stacking along the *b* direction. Both phases maintain orthogonal face-centered scandium sublattices (Fig. S7). The elongated interstitial electrons surround Sc atoms, with only two of three Cl atoms per unit formula matching in space. The electron band structures of *Cmcm*-$ScCl_3$ at 50 GPa and *Amm*2-$ScCl_3$ at 240 GPa are displayed in Fig. S8. The elemental projection electron bands of these two binary compounds are oppositely distributed near the Fermi level, showing obvious traditional ionic properties. Strong ionic interactions reduce the energy of the Cl sublattice bands relative to the Fermi energy level. The phase transition from *Cmcm* to *Amm*2 phase corresponds to the increase of the coordinate number of Sc atoms from 6 in *Cmcm* to 8 in *Amm*2.

The Cl-rich $ScCl_5$ crystallizes in a trigonal *P*-3 structure with four formula units per cell [Fig. 2(f)]. Sc atoms at the corners and edges of the hexagonal lattice form four triangular prisms, and the interstitial sites are occupied by two Sc and two Cl atoms, respectively. The rest Cl atoms are arranged into eight 1D chains crossing around Sc atoms. $ScCl_7$ adopts an A15-derived *Pm*-3 structure at 150 GPa [Fig. 2(g)], featuring two Cl atoms at each lattice face forming Cl chains and an additional isolated central Cl atom in the cubic cell, isostructural with $NaCl_7$ and KCl_7.[11,12] Different from the chlorides $ScCl_{1,2,3}$, where the Cl atoms are all atomic, the Cl-rich binaries ($ScCl_5$ and $ScCl_7$) contain Cl chains with Cl–Cl distances (d_{Cl-Cl}) of 2.08–2.11 Å at 200 GPa, comparable to that in Cl_2 at 1 atm (2.01 Å).[32] The ELFs of *P*-3-$ScCl_5$ and

Pm-3-$ScCl_7$ (Fig. S9) demonstrate the electron accumulation between these adjacent Cl atoms in their Cl chains. Integrated crystal orbital Hamiltonian population (ICOHP)[34,35] analysis between these Cl atoms ranges from −1.50 eV to −1.80 eV in $ScCl_5$ and −1.64 eV to −1.92 eV in $ScCl_7$ per Cl–Cl pair, respectively. All these results indicate the existence of weak covalent interactions and the formation of Cl–Cl covalent homobonds. The interstitial electrons of Sc sublattices in *P*-3-$ScCl_5$ and *Pm*-3-$ScCl_7$ distribute between the Cl atoms with the shortest d_{Cl-Cl} in Cl chains. The Cl atoms in chains show reduced oxidability due to covalent hybridization and form chain motifs through the covalent interactions and chemical template effects provided by the interaction between Sc sublattices' interstitial electrons and Cl (Fig. S9), similar to those in caged-like polyhydrides. Hence, in addition to the contribution from sublattice interactions, the pressure-enhanced Cl–Cl homobonding also plays a key role in governing the stability of these Cl-rich phases, which is similar to observations in polyhydrides and fluorides.[1] Notably, increasing pressure to 300 GPa reduces the d_{Cl-Cl} to 1.99–2.01 Å in both compounds, accompanied by enhanced ICOHP values (−1.78 eV to −2.06 eV in $ScCl_5$ and −1.89 eV to −2.11 eV in $ScCl_7$), indicating strengthened covalent interactions under pressure.

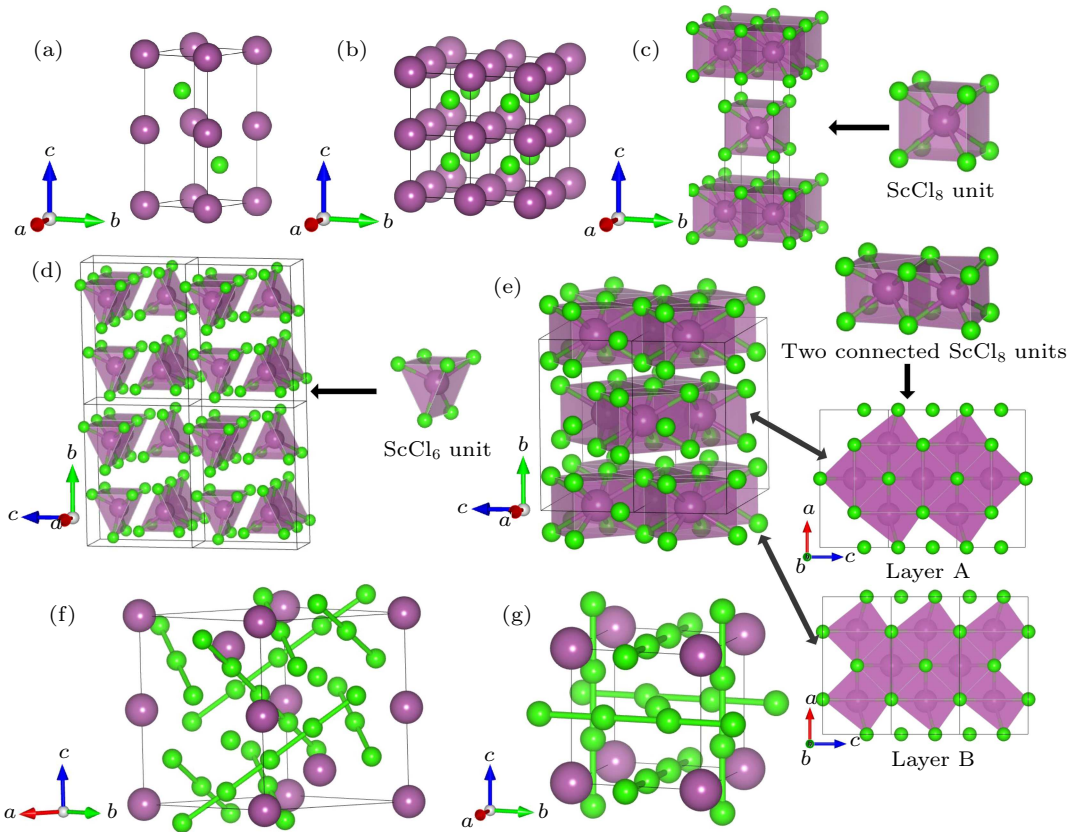


Fig. 2. The crystal structures of (a) *P*6$_3$/*mmc*-ScCl, (b) *Pm*-3*m*-ScCl, (c) *I*4/*mmm*-$ScCl_2$, (d) *Cmcm*-$ScCl_3$, (e) *Amm*2-$ScCl_3$, (f) *P*-3-$ScCl_5$, and (g) *Pm*-3-$ScCl_7$. Scandium atoms are colored purple; chloride atoms are in green.

The comprehensive investigation of thermodynamic stabilities reveals complicated pressure-induced chemistry in the Sc–Cl system. Three fundamental mechanisms govern their thermodynamic stability: classical ionic interactions, metal-nonmetal sublattice crystal orbital matching, and pressure-induced Cl–Cl homonuclear bonding.

Strong ionic interactions clearly play an important role in the stabilization of various Sc–Cl systems, while sublattice orbital interactions and the Cl–Cl homonuclear bonding provide key insights into the elucidation of the pressure dependence of the ground state structure as well as the formation of binary chlorides. Phonon calculations confirm the dynamic stability of all predicted structures as evidenced by the absence of imaginary frequencies in their calculated phonon band structures across the entire first Brillouin zone (Fig. S10).

3.2. Electronic structures and superconductivity

Given the ferromagnetic nature of the atmospheric phase *R*-3*m*-ScCl, we investigated the magnetic properties of the novel high-pressure phases *P*6$_3$/*mmc*-ScCl and *Pm*-3*m*-ScCl. Spin-polarized calculations reveal that these new high-pressure phases of ScCl are nonmagnetic within their thermodynamically stable pressure ranges (Fig. S11). $ScCl_7$ with odd numbers of electrons is also calculated to be nonmagnetic, as shown in Fig. S12. In addition, the spin–orbital coupling (SOC) effect shows an ignorable influence on the Sc–Cl system (Fig. S13). Electron band structures and partial electronic density of states (PDOS) shown in Fig. S14 reveal the metallic

character of all polychlorides except *Cmcm*-$ScCl_3$, with most compounds exhibiting poor metallicity characterized by pseudogaps at the Fermi levels. But for *Pm*-3-$ScCl_7$, a van Hove peak appears near the Fermi level, suggesting potential superconductivity.

These features inspired us to investigate the superconductive properties of metallic chlorides under pressure. We calculated their T_cs using the Allen–Dynes–modified McMillan equation,[31] as shown in Table 1. *Amm*2-$ScCl_3$, *P*-3-$ScCl_5$, and *Pm*-3-$ScCl_7$ are superconductive in corresponding thermodynamically stable pressure ranges, but the calculated T_c values are rather low (Table 1).

To find out the reason for the low T_c, we further calculate the Eliashberg spectral functions $\alpha^2F(\omega)$ and the integral EPC parameters λ as functions of frequencies of the superconductive polychlorides at corresponding pressures (Fig. 3). For *Amm*2-$ScCl_3$ at 220 GPa, the parameters λ and ω_{log} are about 0.33 and 466.86 K, respectively. The whole phonon vibration frequency region is dominated by Cl atoms and a comparable contribution by Sc. The $\alpha^2F(\omega)$ reveals the largest contribution, about 87.99% from the middle-frequency region

Table 1. The calculated EPC parameter (λ), logarithmic average phonon frequency (ω_{log}), critical temperature with $\mu^* = 0.10$ and 0.13 (T_c), and electron density of states at the Fermi level ($N(E_F)$, states/spin/Ry/unit cell), for $P6_3/mmc$-ScCl, *Pm*-3*m*-ScCl, *Amm*2-$ScCl_3$, *P*-3-$ScCl_5$, *Pm*-3-$ScCl_7$, *Pm*-3-$NaCl_7$, and *Pm*-3-KCl_7 at given pressures.

		λ	ω_{log}	T_c	$N(E_F)$
$P6_3/mmc$-ScCl	0 GPa	0.38	233.93	0.25–0.67	7.15
	50 GPa	0.19	422.66	0.00–0.00	4.25
Pm-3*m*-ScCl	0 GPa	0.45	218.92	0.92–1.72	8.25
	100 GPa	0.24	479.18	0.00–0.00	4.57
*Amm*2-$ScCl_3$	150 GPa	0.34	394.34	0.17–0.59	5.43
	220 GPa	0.33	466.86	0.15–0.58	4.99
	300 GPa	0.33	527.34	0.14–0.56	4.55
P-3-$ScCl_5$	75 GPa	0.65	224.34	2.86–3.88	10.53
	200 GPa	0.31	454.33	0.05–0.26	7.07
	300 GPa	0.28	558.39	0.02–0.14	6.66
Pm-3-$ScCl_7$	75 GPa	0.89	192.08	9.09–10.91	19.84
	200 GPa	0.35	488.16	0.28–0.89	13.87
	300 GPa	0.31	579.48	0.07–0.35	12.14
Pm-3-$NaCl_7$	100 GPa	0.65	310.36	6.56–8.88	17.18
	200 GPa	0.38	489.92	0.60–1.54	12.30
	300 GPa	0.31	587.33	0.08–0.41	10.01
Pm-3-KCl_7	125 GPa	0.66	318.68	7.02–9.45	16.68
	200 GPa	0.44	461.39	1.64–3.20	13.39
	300 GPa	0.36	565.71	0.38–1.15	11.07

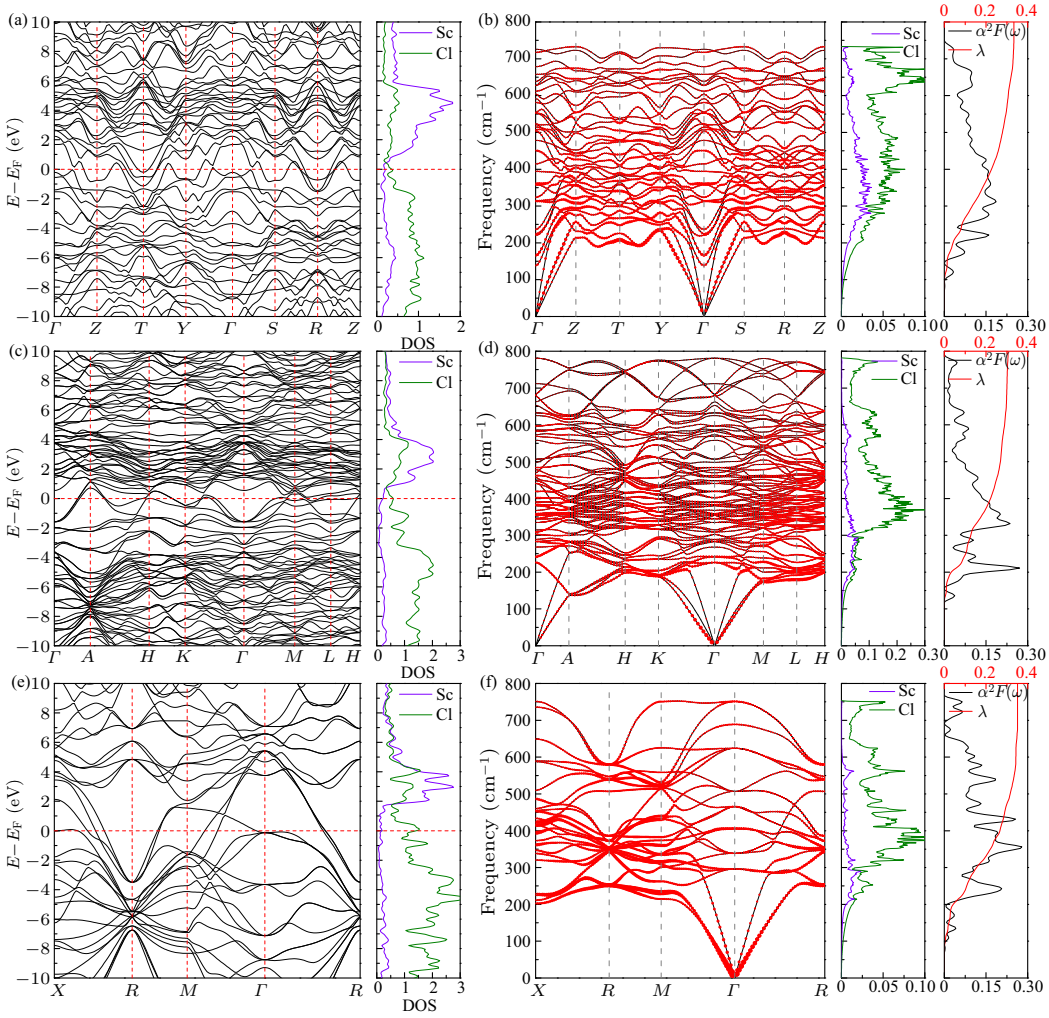


Fig. 3. The electronic band structures and PDOS (left), phonon band structure, PHDOS, and Eliashberg spectral function $\alpha^2F(\omega)$ (right) for (a), (b) *Amm*2-$ScCl_3$ at 220 GPa, (c), (d) *P*-3-$ScCl_5$ at 200 GPa, and (e), (f) *Pm*-3-$ScCl_7$ at 200 GPa. Red solid circles indicate the electron–phonon parameter $\lambda_{q,j}(\omega)$ of each mode (q, j). The radii of red solid circles are proportional to their respective strengths. The integral EPC parameter λ as a function of frequency is calculated and shown in red solid lines.

(147–602 cm^{-1}) to the EPC. *P*-3-$ScCl_5$ and *Pm*-3-$ScCl_7$ display tripartite phonon vibration regions: the low-frequency region equally contributed by the vibrations of Cl and Sc atoms, the middle-frequency region mainly dominated by Cl atoms and a small amount by Sc, and the high-frequency region only from Cl atoms. At 200 GPa, the parameters λ and ω_{log} of *P*-3-$ScCl_5$ and *Pm*-3-$ScCl_7$ are about 0.31, 454.33 K and 0.35, 488.16 K, respectively. The middle-frequency regions (295–672 cm^{-1} and 297–637 cm^{-1}) contribute most to λ about 56.74% and 63.23%, respectively, proving the critical role of the Cl atoms in superconductivities. The relatively low T_c values, compared to analogous $XeCl_n$[36] compounds (9.0 K and 4.3 K for XeCl and $XeCl_2$ with λ about 0.6 and 0.5), arise from reduced λ attributable to a lower density of states at the Fermi level ($N(E_F)$).

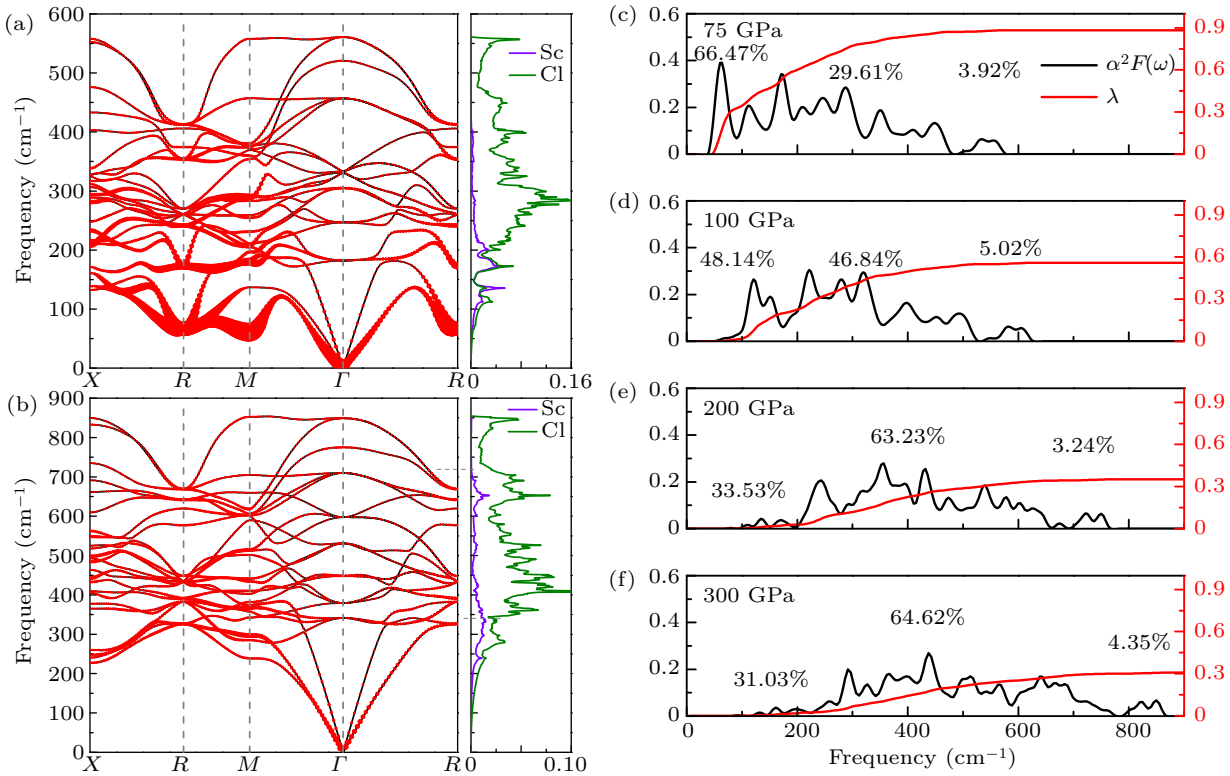


Fig. 4. The phonon band structure (right) and PHDOS (left) of *Pm*-3-$ScCl_7$ at (a) 75 GPa and (b) 300 GPa. (c)–(f) The Eliashberg spectral function $\alpha^2F(\omega)$ (black solid lines) for *Pm*-3-$ScCl_7$ in the pressure range from 75 GPa to 300 GPa. Red solid circles indicate the electron–phonon parameter $\lambda_{q,j}(\omega)$ of each mode (q, j). The radii of red solid circles are proportional to their respective strengths. The integral EPC parameter λ as a function of frequency is calculated and shown in red solid lines. The contributions of the low-, middle-, and high-frequency regions to λ are illustrated in percentages.

The pressure effects on the superconductivity of $ScCl_n$ are also investigated (Table 1). Notably, though $P6_3/mmc$-ScCl and *Pm*-3*m*-ScCl are synthesized under high pressure, they can maintain dynamic stability at ambient pressure as metastable phases, confirmed by phonon calculations (Fig. S15). Large energy barriers of phase transition between atmospheric phase *R*-3*m*-ScCl and high-pressure phases $P6_3/mmc$-ScCl are also found, further confirming the metastabilities of $P6_3/mmc$-ScCl under ambient conditions (Fig. S16). The high-pressure phases $P6_3/mmc$-ScCl and *Pm*-3*m*-ScCl are normal metallic in high-pressure ranges; however, they are superconductive when decompressed to ambient pressure with T_c of 0.25–0.67 K and 0.92–1.72 K, respectively. In addition, ELF analysis (Fig. S17) demonstrates electron accumulation at interstitial 4*f* and 3*d* Wyckoff positions in $P6_3/mmc$-ScCl and *Pm*-3*m*-ScCl structures, respectively, indicating their transition from normal metals to electrides when decompressing to ambient pressure. Therefore, the high-pressure phases $P6_3/mmc$-ScCl and *Pm*-3*m*-ScCl become novel superconductive electrides as pressure decreases to ambient pressure. *Amm*2-$ScCl_3$ and *P*-3-$ScCl_5$ show negligible pressure responses (Figs. S19 and S20) with negligible T_c enhancements of 0.03 K and 3 K upon decompression, respectively. *Pm*-3-$ScCl_7$ exhibits remarkable pressure sensitivity (Table 2) featured by a dramatic increment of T_c from 0.07–0.35 K at 300 GPa to 9.09–10.91 K at 75 GPa, comparable to the 9 K of XeCl at 100 GPa[36] and 13 K of Cl_2 solid at 380 GPa.[23] The enhanced superconductivity in decompressed *Pm*-3-$ScCl_7$ correlates with increased λ (from 0.31 to 0.89) despite decreased ω_{log} (from 579.48 K to 192.08 K). Analysis of mode-specific EPC $\lambda_{q,j}(\omega)$ reveals pronounced phonon softening along the *X*–*R*–*M* path in *Pm*-3-$ScCl_7$ at 75 GPa (Fig. 4), where low-frequency modes below 190 cm^{-1} dominate the coupling strength (Table 2), contributing 66.47% to the total EPC parameter λ with the low-

frequency EPC parameter λ_{low} about 0.59. Under compression to 300 GPa, the progressive suppression of phonon softening leads to diminished total EPC, manifested by a reduced contribution (31.03%) from modes below 342 cm^{-1} to λ, with the λ_{low} decreasing to 0.10. Pressure-dependent Bader charges and ICOHP analyses of *Pm*-3-$ScCl_7$ reveal reduced charge transfer from Sc to Cl ($-1.77e$ to $-1.45e$), and strengthened Cl–Cl covalent interactions (-1.09 eV to -1.92 eV) under compression. This evolution of electronic and phonon band structures suggests a pressure-induced reduction of Cl electronegativity and electron localization within Cl_2 units, weakening metallicity, hardening phonon band structures, and suppressing electron–phonon coupling.

Table 2. The calculated EPC parameter (λ) from low-, middle-, and high-frequency regions of *Pm*-3-$ScCl_7$ at given pressures.

Pressure (GPa)	λ_{low}	ω_{low} (cm^{-1})	λ_{middle}	ω_{middle} (cm^{-1})	λ_{high}	ω_{high} (cm^{-1})	λ
75	0.59	0–190	0.26	190–419	0.04	> 419	0.89
100	0.27	0–222	0.26	222–474	0.03	> 474	0.56
200	0.12	0–296	0.22	296–637	0.01	> 637	0.35
300	0.10	0–342	0.20	342–716	0.01	> 716	0.31

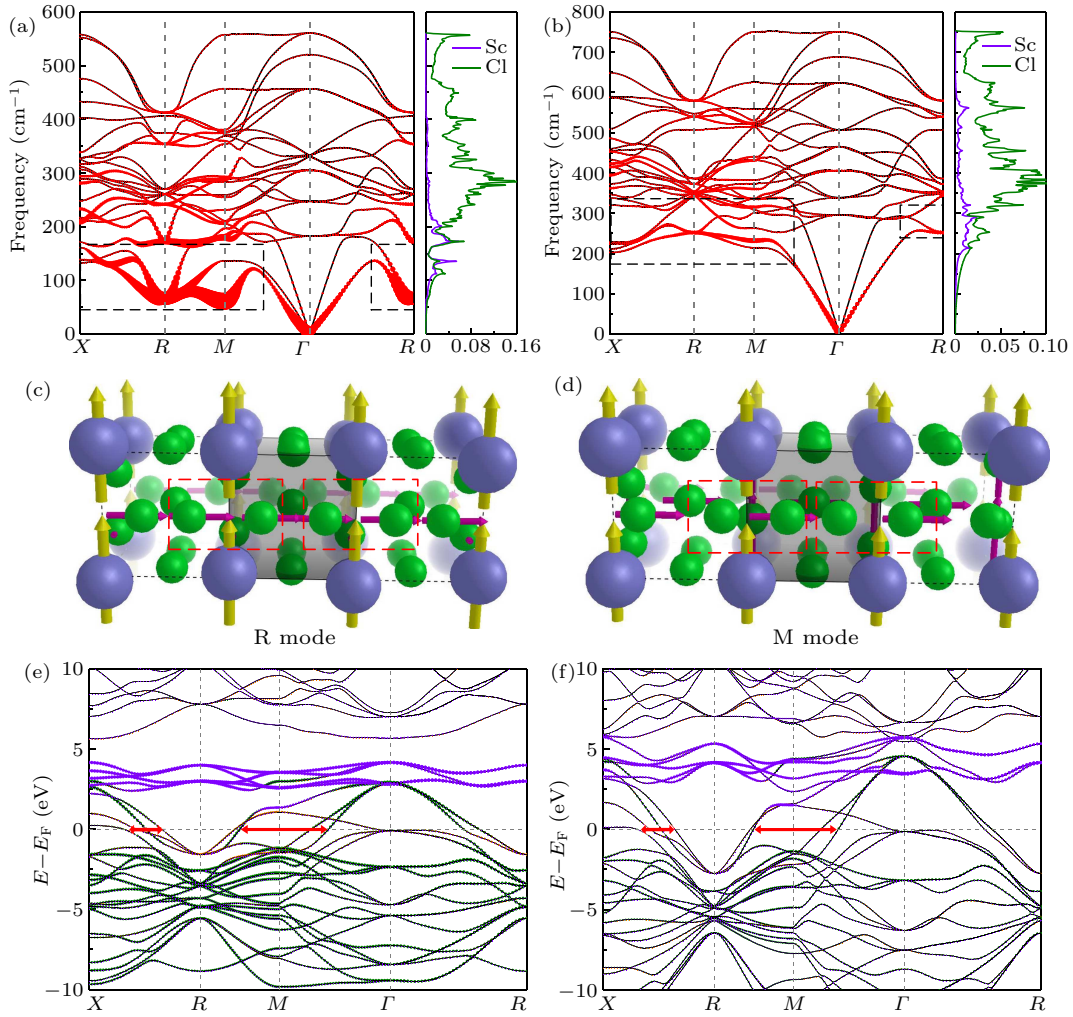


Fig. 5. The phonon band structure (right) and PHDOS (left) of *Pm*-3-$ScCl_7$ at (a) 75 GPa and (b) 200 GPa. Red solid circles indicate the electron–phonon parameter $\lambda_{q,j}(\omega)$ of each mode (q, j). The radii of red solid circles are proportional to their respective strengths. The black dashed rectangular dashed boxes mark the modes with phonon softening. (c) and (d) The representative phonon modes contribute to the phonon softening. The large purple balls and small green balls represent metal atoms and Cl atoms, respectively. The red dashed rectangular dashed boxes mark the Cl_2 units with the same vibration behaviors. (e) and (f) The band structures of *Pm*-3-$ScCl_7$ with projections of Sc (violet solid circles), Cl atoms in chains (olive solid circles), and Cl atoms at body centers (red solid circles) at 75 GPa (left), and 200 GPa (right), respectively. The red arrows mark the electron bands with parallel characters crossing the Fermi level. The Fermi level is set to zero.

The atomic vibration modes corresponding to phonon softening regions are visualized in Fig. 5. These softening modes, contributing predominantly to the electron–phonon coupling (EPC) parameter, originate chiefly from stretching vibrations between Cl_2 units within chlorine atomic chains along three perpendicular directions. Electron band structures at the Fermi level are dominated by Cl atoms. Particularly along k-paths exhibiting phonon softening, bands crossing the

Fermi level display parallel dispersion, indicating Fermi surface nesting. Increasing pressure gradually hardens phonon vibrations while reducing electronic states at the Fermi level — especially those responsible for nesting — thereby diminishing EPC. Thus, the superconductivity of *Pm*-3-$ScCl_7$ primarily stems from EPC generated by vibrations of the chlorine chain.

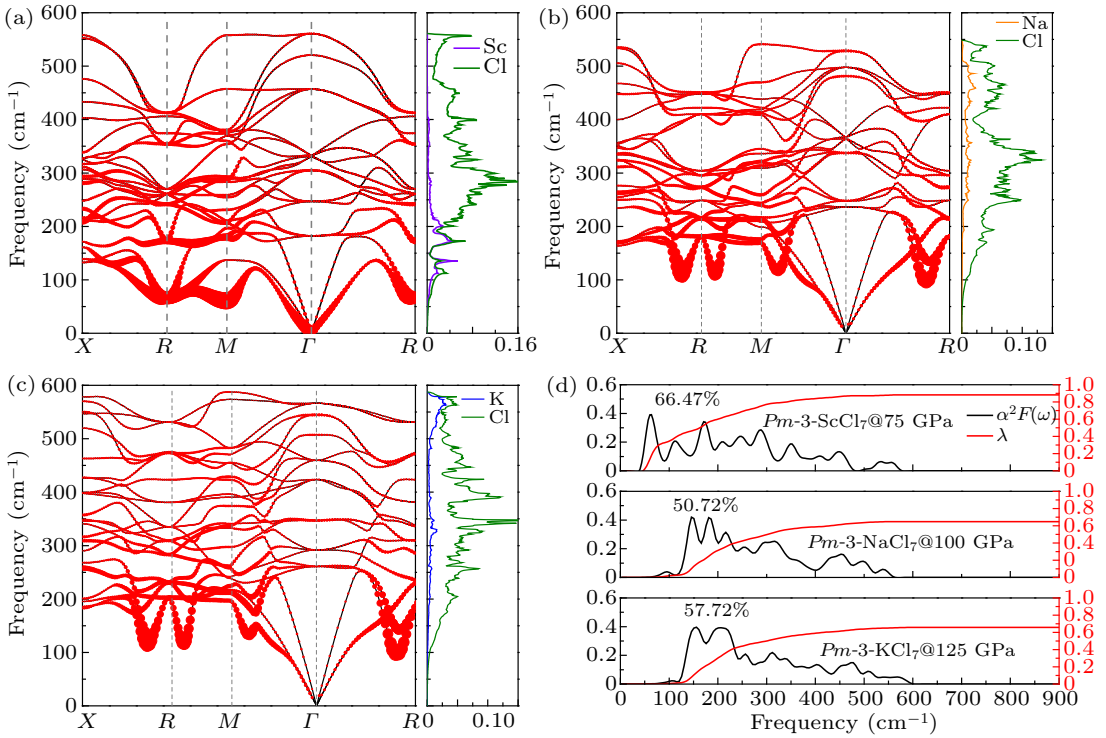


Fig. 6. The phonon band structure (right) and PHDOS (left) of (a) *Pm*-3-$ScCl_7$ at 75 GPa, (b) *Pm*-3-$NaCl_7$ at 100 GPa, and (c) *Pm*-3-KCl_7 at 125 GPa. (d) The Eliashberg spectral function $\alpha^2F(\omega)$ (black solid lines) for *Pm*-3-$ScCl_7$ at 75 GPa (up), *Pm*-3-$NaCl_7$ at 100 GPa (middle), and *Pm*-3-KCl_7 at 125 GPa (down). Red solid circles indicate the electron–phonon parameter $\lambda_{q,j}(\omega)$ of each mode (q, j). The radii of red solid circles are proportional to their respective strengths. The integral EPC parameter λ as a function of frequency is calculated and shown in red solid lines. The contributions of the low-frequency regions to λ are illustrated in percentages.

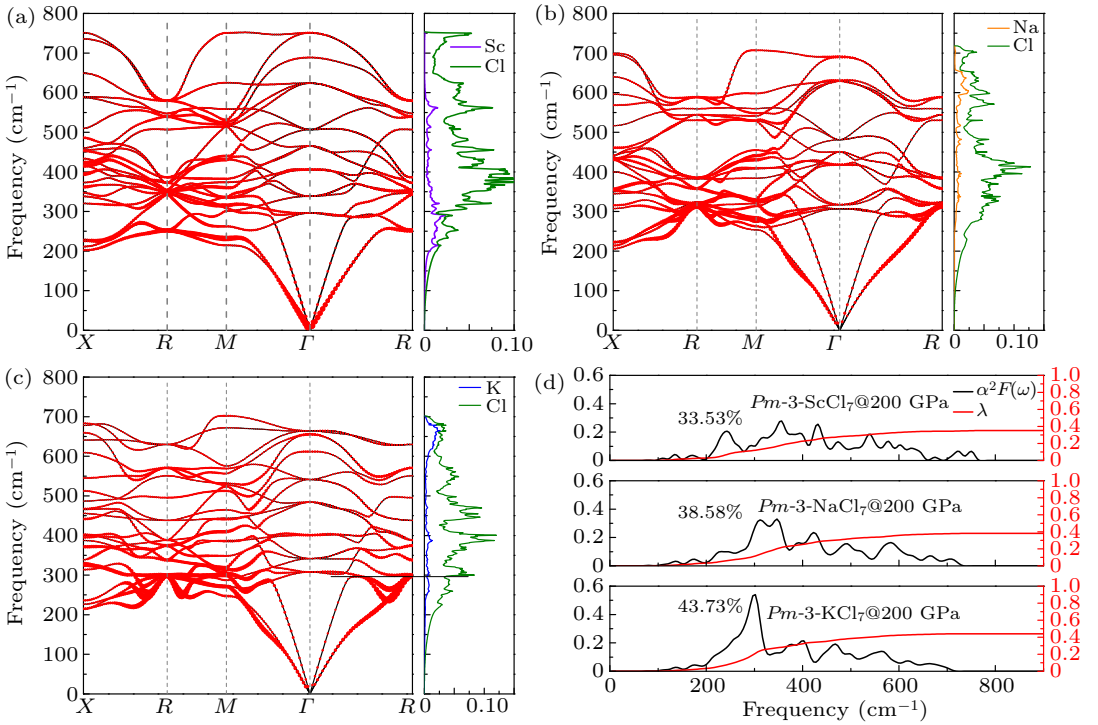


Fig. 7. The phonon band structure (right) and PHDOS (left) of (a) *Pm*-3-$ScCl_7$, (b) *Pm*-3-$NaCl_7$, and (c) *Pm*-3-KCl_7 at 200 GPa. (d) The Eliashberg spectral function $\alpha^2F(\omega)$ (black solid lines) for *Pm*-3-$ScCl_7$ (up), *Pm*-3-$NaCl_7$ (middle), and *Pm*-3-KCl_7 (down) at 200 GPa. Red solid circles indicate the electron–phonon parameter $\lambda_{q,j}(\omega)$ of each mode (q, j). The radii of red solid circles are proportional to their respective strengths. The integral EPC parameter λ as a function of frequency is calculated and shown in red solid lines. The contributions of the low-frequency regions to λ are illustrated in percentages.

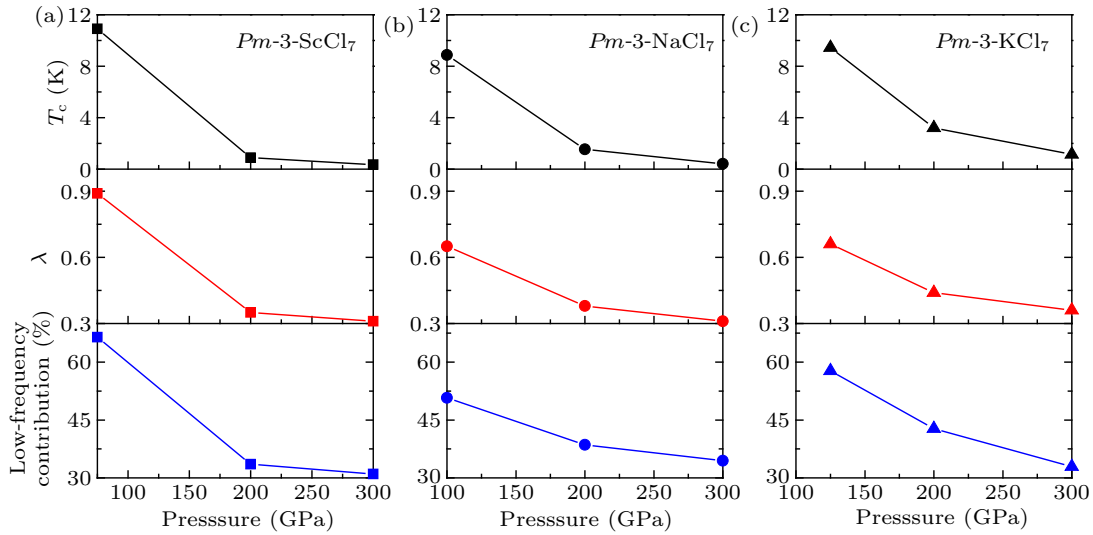


Fig. 8. The pressure-dependent evolution of T_c (black), EPC parameters λ (red), and contribution from low-frequency regions to EPC (blue) of (a) *Pm*-3-ScCl$_7$, (b) *Pm*-3-NaCl$_7$, and (c) *Pm*-3-KCl$_7$.

The isostructural compounds *Pm*-3-NaCl$_7$[12] and *Pm*-3-KCl$_7$[11] display similar pressure-dependent superconductivity (Table 1). Previous researches demonstrate the thermodynamic stabilities of *Pm*-3-NaCl$_7$ and *Pm*-3-KCl$_7$ above 142 GPa and 225 GPa, respectively. *Pm*-3-NaCl$_7$ shows T_c enhancement from 0.08–0.41 K at 300 GPa to 6.56–8.88 K at 100 GPa, and *Pm*-3-KCl$_7$ exhibits an increase from 0.38–1.15 K at 300 GPa to 7.02–9.45 K at 125 GPa, with corresponding λ increases from 0.31 to 0.65 and 0.36 to 0.66. This systematic behavior suggests the *Pm*-3 structure type represents a general framework for pressure-tunable chloride superconductors.

Similar to *Pm*-3-ScCl$_7$, EPC parameter λ in *Pm*-3-NaCl$_7$ and *Pm*-3-KCl$_7$ arises mainly from low-frequency phonon softening along *X*–*R* and *R*–*M* directions (Fig. 6). Low-frequency regions dominate λ of NaCl$_7$ and KCl$_7$ with contributions of 50.72% and 57.72% at 100 GPa and 125 GPa, respectively. PHDOS confirms low-frequency modes correspond to Cl-atom vibrations, indicating major EPC contributions from chlorine. Figure S21 schematics reveal that phonon softening modes primarily involve stretching vibrations between Cl_2 units within 1D chains. At 300 GPa, phonon softening vanishes with superconductivity suppression. Comparing T_c values of ScCl$_7$ (0.28–0.89 K), NaCl$_7$ (0.60–1.54 K), and KCl$_7$ (1.64–3.20 K) at 200 GPa confirms that T_c primarily follows λ trends (Fig. 7). Low-frequency contributions induced by phonon softening critically determine λ. KCl$_7$ with the highest λ shows 43.73% contribution below 296.72 cm^{-1}, while ScCl$_7$ with the lowest λ exhibits 33.53% below 297.56 cm^{-1}. Metal-atom vibrations demonstrate negligible influence, consistent with our results on superconductivity of *Pm*-3-ScCl$_7$. The Cl-chain vibrations dominate EPC and pressure-dependent superconductivity in *Pm*-3-MCl$_7$ chlorides, which is displayed in Fig. 8 as a summary.

4. Conclusion

Using first-principles calculations combined with evolutionary algorithm structural predictions, we systematically investigate the phase diagram of scandium polychlorides from 50 GPa to 300 GPa, establishing the thermodynamic stabilities of ScCl, $ScCl_2$, $ScCl_3$, $ScCl_5$, and ScCl$_7$. Apart from strong ionic interactions, the sublattice orbital interactions and formation of Cl–Cl homobonds emerge as critical determinants for elucidating both pressure-modulated phase transformations and unconventional chloride stoichiometry formation. Remarkably, the high-pressure *P*6$_3$/*mmc*-ScCl and *Pm*-3*m*-ScCl phases retain metastability at ambient conditions, exhibiting intermetallic electride and superconducting properties. Furthermore, superconductivity observed in *Pm*-3-ScCl$_7$ shows enhanced transition temperatures at lower pressures, attributed to weakened Cl–Cl bonds, phonon softening, and increased EPC. The discovery of superconductivity across *Pm*-3 structured chlorides suggests this structural type may serve as a prototype for pressure-tunable superconductors.

Acknowledgements

This work was supported by the "Pioneer" and "Leading Goose" R&D Program of Zhejiang Province (Grant No. 2022C01053), Zhejiang Provincial Natural Science Foundation of China (Grant No. LQ23A040010), the Open Fund of the State Key Laboratory of Spintronics Devices and Technologies (Grant No. SPL-2404), Zhejiang Provincial Natural Science Foundation of China (Grant No. Y24F050044). D. D. acknowledges the National Natural Science Foundation of China (Grant Nos. 12274169 and 12122405). M. M. acknowledges NSF DMR 1848141, OAC 2117956, the Camille and Henry Dreyfus Foundation, and CSU RSCA grants. Parts of the calculations were performed in the High Performance

Computing Center (HPCC) of TianHe-1(A) at the National Supercomputer Center in Tianjin.

References

[1] Miao M S, Sun Y H, Zurek E and Lin H Q 2020 *Nat. Rev. Chem.* **4** 508
[2] Froyen S and Cohen M L 1984 *Phys. Rev. B* **29** 3770
[3] Sims C E, Barrera G D, Allan N L and Mackrodt W C 1998 *Phys. Rev. B* **57** 11164
[4] Válgoma J A, Perez-Mato J M, García A, Schwarz K and Blaha P 2002 *Phys. Rev. B* **65** 134104
[5] Leger J M and Atouf A 1992 *J. Phys.: Condens. Mat.* **4** 357
[6] Wan B, Lu Y F, Xiao Z W, Muraba Y, Kim J W, Huang D J, Wu L L, Gou H Y, Zhang J W and Gao F M 2018 *NPJ Comput. Mater.* **4** 1
[7] McGuire M A, Clark G, Kc S, Chance W M, Jellison G E, Cooper V R, Xu X D and Sales B C 2017 *Phys. Rev. Mater.* **1** 014001
[8] Cao H B, Banerjee A, Yan J Q, Bridges C A, Lumsden M D, Mandrus D G, Tennant D A, Chakoumakos B C and Nagler S E 2016 *Phys. Rev. B* **93** 134423
[9] Vologzhanina A V, Pushkin D V and Serezhkin V N 2006 *Russ. J. Coord. Chem.* **32** 815
[10] McGuire and A M 2017 *Crystals* **7** 121
[11] Zhang W, Oganov A R, Zhu Q, Lobanov S S, Stavrou E and Goncharov A F 2016 *Sci. Rep.* **6** 26265
[12] Zhang W W, Oganov A R, Goncharov A F, Zhu Q, Boulfelfel S E, Lyakhov A O, Stavrou E, Somayazulu M, Prakapenka V B and Konôpková Z 2013 *Science* **342** 1502
[13] Yang Q P, Zhao K X, Liu H Y and Zhang S T 2021 *J. Phys. Chem. Lett.* **12** 5850
[14] Kong J, Shi K Y, Oganov A R, Zhang J Q, Su L and Dong X 2024 *Matter Radiat. Extremes* **9** 067803
[15] Kong J, Su L, Cui H X, Ding H R, Hou J Y, Chi C X, Liu S Y, Zhou X F, Wang H T and Dong X 2024 *Chin. Phys. Lett.* **41** 107101
[16] Yu H L and Chen Y 2021 *J. Phys.: Condens. Mat.* **33** 215401
[17] Sun Y H and Miao M S 2023 *Chem* **9** 443
[18] Sun Y, Zhao L, Pickard C J, Hemley R J, Zheng Y and Miao M 2023 *Proc. Natl. Acad. Sci. USA* **120** e2218405120
[19] Ye X Q, Zarifi N, Zurek E, Hoffmann R and Ashcroft N W 2018 *J. Phys. Chem. C* **122** 6298
[20] Qian S F, Sheng X W, Yan X Z, Chen Y M and Song B 2017 *Phys. Rev. B* **96** 094513
[21] Abe K 2017 *Phys. Rev. B* **96** 144108
[22] Rahm M, Cammi R, Ashcroft N W and Hoffmann R 2019 *J. Am. Chem. Soc.* **141** 10253
[23] Li P F, Gao G Y and Ma Y M 2012 *J. Chem. Phys.* **137** 064502
[24] Oganov A R and Glass C W 2006 *J. Chem. Phys.* **124** 244704
[25] Lyakhov A O, Oganov A R, Stokes H T and Zhu Q 2013 *Comput. Phys. Commun.* **184** 1172
[26] Perdew J P, Burke K and Ernzerhof M 1996 *Phys. Rev. Lett.* **77** 3865
[27] Kresse G and Furthmüller J 1996 *Comp. Mater. Sci.* **6** 15
[28] Kresse G and Joubert D 1999 *Phys. Rev. B* **59** 1758
[29] Giannozzi P, Baroni S, Bonini N, Calandra M, Car R, Cavazzoni C, Ceresoli D, Chiarotti G L, Cococcioni M, Dabo I, Dal Corso A, de Gironcoli S, Fabris S, Fratesi G, Gebauer R, Gerstmann U, Gougoussis C, Kokalj A, Lazzeri M, Martin-Samos L, Marzari N, Mauri F, Mazzarello R, Paolini S, Pasquarello A, Paulatto L, Sbraccia C, Scandolo S, Sclauzero G, Seitsonen A P, Smogunov A, Umari P and Wentzcovitch R M 2009 *J. Phys.: Condens. Mat.* **21** 395502
[30] Methfessel M and Paxton A T 1989 *Phys. Rev. B* **40** 3616
[31] Allen P B and Dynes R C 1975 *Phys. Rev. B* **12** 905
[32] Dalladay Simpson P, Binns J, Peña Alvarez M, Donnelly M E, Greenberg E, Prakapenka V, Chen X J, Gregoryanz E and Howie R T 2019 *Nat. Commun.* **10** 1134
[33] Akahama Y, Fujihisa H and Kawamura H 2005 *Phys. Rev. Lett.* **94** 195503
[34] Dronskowski R and Bloechl P E 1993 *J. Phys. Chem.* **97** 8617
[35] Maintz S, Deringer V L, Tchougréeff A L and Dronskowski R 2016 *J. Comput. Chem.* **37** 1030
[36] Zarifi N, Liu H Y, Tse J S and Zurek E 2018 *J. Phys. Chem. C* **122** 2941